remote sensing

MDPI

Assessing the predictive power of Democratic Republic of Congo's LiDAR-based biomass map over independent test samples

Lamulamu A.[1,*], Ploton P.[2,*], Birigazzi L.[3], Xu L.[4], Saatchi S.S.[4,5] and Kibambe Lubamba J.P.[1,6]

1. Faculté des Sciences Agronomiques, Département de Gestion des Ressources Naturelles, Université de Kinshasa, Kinshasa, Democratic Republic of the Congo
2. AMAP, Univ Montpellier, IRD, CNRS, INRAE, CIRAD, Montpellier, France
3. Forestry Consultant, Via Unione Sovietica 105, Grosseto, Italy
4. Institute of Environment and Sustainability, University of California, Los Angeles, CA, USA
5. Jet Propulsion Laboratory, California Institute of Technology, Pasadena, CA, USA
6. Wildlife Conservation Society, Kinshasa, Democratic Republic of the Congo
*. These authors contributed equally

ABSTRACT: Remotely sensed maps of forest carbon stocks have enormous potential for supporting greenhouse gas (GHG) inventory and monitoring in tropical countries. However, most countries have not used maps as the reference data for GHG inventory due to the lack of confidence in the accuracy of maps and of data to perform local validation. Here, we use the first national forest inventory (NFI) data of the Democratic Republic of Congo (DRC), to perform an independent assessment of the country's latest high-resolution LiDAR-based carbon stocks map. We compared plot-to-plot variations and areal estimates of forest aboveground biomass (AGB) derived from NFI data and from the map across jurisdictional and ecological domains. Across all plots, map predictions were nearly unbiased and captured c. 60% of the variation in NFI plots AGB. Map performance was not uniform along the AGB gradient, and saturated around c. 290 $Mg.ha^{-1}$, increasingly underestimating forest AGB above this threshold. Splitting NFI plots by land cover types, we found map predictions unbiased in the dominant *terra firme* Humid forest class, but weakly captured plot-to-plot variations (R^2 of c. 0.33, or c. 0.20 after excluding perturbed plots). In contrast, map predictions underestimated AGB by c. 33% in the low-AGB Woodland savanna class, but captured a much greater share of plot-to-plot AGB variation (R^2 of c. 0.41, or 0.58 after excluding perturbed plots). Areal estimates from the map and NFI data depicted a similar trend with a slightly lower (but statistically indiscernible) mean AGB from the map across the entire study area (i.e., 252.7 vs 280.6 $Mg.ha^{-1}$) owing to the underestimation of mean AGB in the Woodland savanna domain (31.8 vs 57.3 $Mg.ha^{-1}$), which was broadly consistent with the results obtained at provincial level. This study provides insights and outlooks for the computation of emission factors in DRC for REDD+.

Keywords: Satellite Remote Sensing; Aboveground Biomass; UNFCCC REDD+; Democratic Republic of Congo

Citation: Lastname, F.; Lastname, F.; Lastname, F. Title. *Remote Sens.* **2022**, *14*, x. https://doi.org/10.3390/xxxxx

Academic Editor: Firstname Lastname

Received: date
Accepted: date
Published: date

1. Background

The Congo Basin hosts the second largest block of continuous tropical dense forests on Earth, and thus plays an important role in global carbon and climate systems [1]. Direct threats to these forests include in particular smallholder agriculture, unsustainable forest logging, fuelwood energy consumption and carbonization that are exacerbated by the rapid population growth, the lack of efficient land use planning and the weak governance in the forestry sector [2]. In the Democratic Republic of Congo (DRC) for instance, which is home to the largest share of the basin's forests, the deforestation rate has been increasing since the early 2000s, from ca. 0.9% between 2000 and 2010 to ca. 1.3% between 2010 and

2014 [3]. Everything being equal as observed over the last two decades, the DRC deforestation trend will most likely increase in the coming years as 80-90% of DRC's deforestation is driven by small-scale clearing for subsistence agriculture [2,3], while the population is forecasted to increase by more than height fold between 2000 and 2100 [4]. In this context of a growing pressure on tropical forests and of international concerns about climate change, initiatives to curb tropical forest carbon emissions have emerged, such as the Reducing Emissions from Deforestation and forest Degradation (REDD+) scheme in which the DRC has been engaged since 2009 [3,5].

REDD+ implementation requires participating countries to monitor forest carbon emissions at national scale following a set of good practices that warrant the transparency, completeness and accuracy of the results. The general methodology of such monitoring system usually amounts to quantifying forest cover changes between consecutive monitoring dates (i.e., activity data) and to infer associated carbon dioxide emissions (or absorptions) by multiplying activity data with emission factors [6]. In this computation workflow, emission factors represent the largest source of uncertainty on carbon emission estimates [7] due to the uncertainty on forest carbon stocks prior to landcover change [8]. Indeed, in contrast with Northern countries where ground-based forest resource assessment is a long-standing tradition [9], much less forest inventory data is available in tropical countries. In fact, National Forest Inventories are still challenging for many tropical developing countries [7], including DRC, due to several reasons such as the lack of adequate infrastructure, human resource and financial constraints and security issues. Improving our understanding of the spatial distribution of tropical forest carbon stock thus remains a central stake to constrain uncertainties on carbon emissions, help tropical countries to fully operationalize the REDD+ process and inform forest management decision-making.

Spaceborne remote-sensing (RS) is seen as a key tool for country-wide, repeated monitoring of the spatial distribution of forest carbon stocks using limited ground inventories [8]. However, broad-scale remote sensing studies of forest carbon stocks – or its proxy, namely the aboveground biomass (AGB) – cope with large sources of uncertainty in the AGB mapping chain [10]. AGB mapping uncertainty might result from several factors including (1) the paucity of data available to calibrate and validate RS models, (2) difficulties to link field and RS data (mismatch in spatial resolutions [11], edge effect [12], geolocation uncertainty [13], etc.), (3) the map over-estimation of low AGB values [14,15] and (4) the saturation of current wall-to-wall RS data leading to underestimating high-AGB values as in dense forests [14,15]. These challenges have not been completely overcome in current pantropical AGB maps which show substantial disparities both in terms of the magnitude of forest biomass at any given place and its variation pattern over space notably in the Congo basin[16]. To date, countries are thus encouraged to favor AGB estimates from national ground-based inventories over broad-scale RS maps for their international greenhouse gas reporting [17]. While improvements of pantropical mapping products are expected in the coming years thanks to recent and upcoming spaceborne missions (GEDI, BIOMASS), a new carbon map is already available for DRC [18]. This map – hereafter referred to as the LiDAR-based biomass map – has been produced using original data and a mapping methodology that should improve the quality of AGB predictions over existing pantropical products. For instance, the mapping model has been trained on a probability sample of hundreds of thousands of hectares of aerial LiDAR data distributed over the entire country. In comparison with spaceborne LiDAR data from the GLAS sensor used to train older pantropical products, the detailed characterization of vegetation structure provided by aerial LiDAR data should provide more accurate reference AGB estimates. Aerial LiDAR data also provide a complete coverage of reference pixels used to train the mapping model, thereby solving the issue of sampling uncertainty introduced by the small size of GLAS shots with respect to the mapping resolution in pantropical studies [19]. Further, LiDAR-derived reference AGB estimates were upscaled using Landsat data, which has a much finer spatial resolution than MODIS data used in pantropical studies (i.e., 30 m vs 500 m) and should therefore allow discerning more variability in forest dynamics to ultimately improve our capabilities to map AGB variation. That being said, while the LiDAR-based biomass map could help DRC to reduce uncertainty on its national emission factors, the aforementioned map has not been subject to an independent validation yet and has thus not been used by the country in its Forest Reference Emission Level [3].

In this study, we leveraged hundreds of field sample plots from the yDRC’s first NFI to perform an independent assessment of the LiDAR-based biomass map [18]. Specifically, we seek to (1) evaluate the map predictive power on biomass variation across all plots and within broad landcover types, and (2) compare population-level mean biomass estimates derived from NFI data with those derived from the map at different spatial scales.

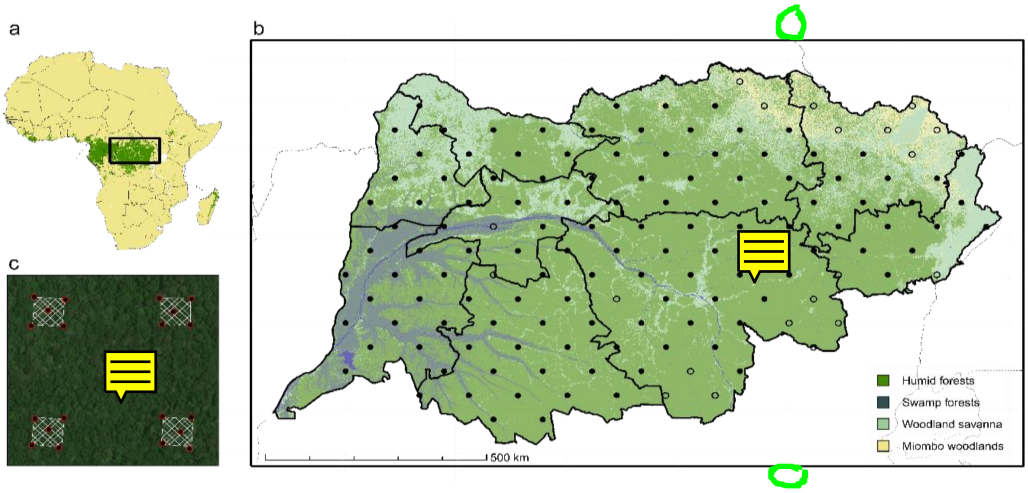

Figure 1. a., Location of the study area (black square) in Africa. **b.,** Spatial distribution of sampling units within the study area. Sampling units that were effectively sampled are represented with filled black circles, while sampling units left unsampled are represented with empty black circles. Thick and thin black lines represent countries and DRC provinces borders, respectively. **c.,** Illustrative example of one sampling unit, composed of four sample plots (white hashed squares). The locations of GPS measurements by plots are represented by red circles. .

2. Materials and methods

2.1. Study area

The study area comprises the nine northern DRC provinces (out of 26 for the whole country), which represents a total size of c. 900,000 km² or about half the country. The climate is characterized by two rainy seasons per year usually starting around March (for two months) and October (for three months). Annual precipitation ranges from 810 to 2,000 mm and annual temperature from 24 to 25 °C. The study area is dominated by forested lands and notably encompasses the vast majority of DRC’s humid forests (Fig. 1-b).

2.2. National Forest Inventory data

2.2.1. Sampling design

The DRC NFI was based on probabilistic sampling principles and used a systematic clustered sampling design. A triangular sampling grid was created and randomly positioned over the country. The grid was composed of isosceles triangles oriented along the N-S axis with bases measuring c. 110 km and equal sides c. 78 km. Each node of the grid was used as the origin of a sampling unit, which was composed of four 75 m x 75 m sample plots spaced out by 250 m (Fig. 1-c) to limit spatial autocorrelation in measurements among plots. The sampling strategy brought a total of 321 sampling units spread over the country area excluding Maï Ndombe, Kwilu and Kwango provinces which were not targeted by the NFI, resulting in a sampling intensity of one sampling unit per c. 6.3 × 10^3 km^2. 143 sampling units were located in the study area among which one was located in the Congo River and 20 were not surveyed by the field teams due to local armed conflicts, notably in the North- and South-Eastern edges of the study area. Among 122 remaining sampling units (representing 488 plots), 11 plots were not sampled due to conflicts with local populations and access difficulties (e.g., strong slopes). Therefore, the total number of plots for this study is 477.

2.2.2. Field data

To perform the field survey, ten field teams were simultaneously deployed by the Forest Inventory and Management Direction ("Direction des Inventaires et Aménagement Forestier", DIAF) of the Minister of Environment and Sustainable Development ("Ministère de l'Environnement et du Développement Durable", MEED). Each team was composed of two forest engineers from DIAF and a trained botanist from the University of Kisangani. Data collection over the study area (Fig. 1-b) corresponded to the first phase of the NFI and was performed between September 2017 and December 2018. For each sampling unit, the origin (S-W corner) of the four plots were provided to the field teams and located in the field using a handheld global positioning system (GPS) device (Garmin 64S). Plot limits were delimited using compasses and measurement tapes. To limit plot geolocation errors and facilitate spatial co-registration with remote sensing products, the geolocation of five locations per plot were recorded (i.e., the four corners and the plot center, Fig. 1-c) by averaging GPS measurements over a few seconds at each location.

Plot measurements followed a standard protocol. Each tree with a diameter at breast height (DBH) ≥ 20 cm was measured and identified, while trees in the 10-20 cm DBH range were sampled on a subset of the plot of size 50 × 25 m. Tree DBH were measured at 1.3 m height, or 30 cm above any buttresses or deformities. The height (H) of c. 50 trees distributed across the DBH range found in the plot were measured using a laser rangefinder device (TruPulse 360R). Herbarium specimens were collected on each tree for which the identification was uncertain and were stored at the Ecology and Forest Management laboratory (LECAFOR) of Kisangani University. The total raw inventory dataset for the study area contains 46,963 tree DBH measurements and 13,365 H measurements. Of the 46,963 trees, 89.5% were identified at the species level, 6.6% at the genus level and 3.9% were left unidentified. Further database screening showed that some tree H measurements within 8 sampling units surveyed by the same field team were unrealistic. All H measurements from those sampling units were thus discarded leaving a total of 12,359 H measurements in the dataset.

Because of the systematic sampling design, some plots overlaid different land cover classes (e.g., humid forest, crops, etc.). For each plot, a sketch was drawn to represent the spatial distribution of land cover classes within the plot, following a detailed classification system containing 15 classes. For the purposes of this analysis, we simplified this classification system, aggregating NFI's land cover classes into six aggregate classes that matched the land cover classification used by DRC in its Forest Reference Emission Levels [3]: savannas, crops, natural regenerations on abandoned crops, dense humid forests on hydromorphic soil, *terra firme* dense humid forests and other forests. This simplified land cover classification was used for the establishment of tree height-diameter (H:D) allometric models (see next section).

2.2.3. Aboveground biomass estimation from inventory data

We used the BIOMASS package (v. 2.1.5.9) in the R statistical platform (v. 4.0.5) to estimate sample plots aboveground biomass and its uncertainty.

The first step of the procedure consisted in attributing a wood density (WD) estimate (and its uncertainty) to each tree in the dataset. This was performed by the *getWoodDensity* function, which relies on WD measurements available in the Global Wood Density database (GWD_{db} [20,21]). For trees identified at species or genus levels, the mean WD of tropical African trees at the appropriate taxonomic level was used. When tree taxonomy was only available at the family level or trees were unidentified, the mean WD of trees found in the same sampling unit and land cover class was used. The *getWoodDensity* function provides for each mean WD estimate the associated uncertainty. This uncertainty is either based on the standard deviation of individual WD measurements used to compute the mean WD (when 10 measurements or more were used) or on the standard deviation of individual WD measurements across the entire database (when less than 10 measurements were used).

Second, we built H:D allometric models to predict the height of trees that were not measured in the field. Given the high spatial variability in H:D relationships [22], we favored local H:D models (e.g. by sampling unit) over more general regional-scale models (e.g. by land cover class). When ≥ 15 H measurements were available for a land cover class within a sampling unit (which represents [illegible] % of the trees), a two-parameter Weibull distribution function was fitted on those trees and used to predict the H of unmeasured trees within the same stratum. For the remaining 8.9% of trees in the dataset, H was predicted with land cover class specific H:D models fitted on the entire dataset. H prediction uncertainty for each tree in the dataset was computed as the residual standard error of the corresponding H:D model.

Third, to account for the partial sampling of trees in the 10-20 cm DBH range, we followed the procedure described in [23]. This procedure is embedded in the Monte Carlo computation scheme described in the subsequent paragraph and allows simulating, for each plot, the missing inventory data (i.e. tree diameters and identifications) for trees in the 10-20 cm DBH range that were not sampled on the entire plot (i.e. so-called Specific functions 1 and 2 in [23]). In practice, this procedure (i) expands the count of trees in the 10-20 cm DBH class from the observed count r in the spatial fraction p of the plot that was actually surveyed to the entire plot area by randomly generating a value from a negative binomial distribution X ~ NegBin(r, p), (ii) assigns species labels to simulated trees at the pro-rata of species abundance observed in the p fraction of the plot and (iii) assigns a continuous diameter to each simulated tree by inverse transform sampling from a two-parameter Weibull distribution function, with a scale parameter $\lambda = 8.593$ and a shape parameter $k = 0.737$.

Fourth, we used a Monte Carlo procedure to compute the AGB of each tree (and its uncertainty) with the pantropical AGB allometric model [24]. The procedure propagates uncertainties arising from the simulation of missing inventory data, WD, H, and the allometric model to tree AGB predictions (see [23] for details). The output of the procedure is a vector of 1,000 AGB replicates per tree. For a given sample plot, the output matrix can thus be summed by Monte Carlo iterations to obtain a vector of 1,000 replicates of plot AGB (i.e., AGB_{iter}, with *iter* in [1-1,000]), which incorporates the different sources of uncertainty. Each AGB_{iter} replicate represents a realization of plot AGB for trees with DBH ≥ 10 cm over the 75 x 75 m plot area. AGB_{iter} replicates were thus standardized to 1-ha to allow for comparison with biomass density values of the LiDAR-based AGB map.

Last, to account for trees in the range of 1-10 cm DBH, we used the model proposed by [18]:

$$AGB_{\geq 1cm} = 1.872 * AGB_{iter}^{0.906} \quad \text{(eq. 1)} \tag{1}$$

Following [18], we assumed that scaling up AGB_{iter} to $AGB_{\geq 1cm}$ propagated a negligible uncertainty. The mean of the $AGB_{\geq 1cm}$ vector was then used as our field estimate of plot AGB (i.e., AGB_{field}).

2.2.4. Linking field plots to LiDAR-based biomass and land cover maps

An important stake when evaluating a map is to accurately position reference data. Under forest canopy, the error on a GPS measurement acquired with a precise receiver commonly exceeds 20 m, and can be as high as 200 m [25]. Reducing plot geolocation errors therefore requires using GPS measurements at multiple locations of the plot, so that random GPS errors average out [13]. For each plot, we thus leveraged all (usually five) GPS measurements to determine the most probable plot geolocation using the *correctCoordGPS* function of the BIOMASS R package. The *correctCoordGPS* function performs a procrust (translation, rotation) on the set of GPS coordinates while preserving plot size (75 m x 75 m) and squared shape. For some plots, a few GPS measurements were either missing or unrealistic (e.g. located ≥ 100 km from the plot center). To avoid introducing errors in the assessment of the LiDAR-based AGB map associated with spatial mismatches between the map and the reference data, we discarded all plots with less than three GPS measurements (n = 7). For the remaining 470 plots, we extracted (i) the area-weighed means of AGB values in the LiDAR-based AGB map (hereafter AGB_{map}) and (ii) the modal class of the land cover map used in the construction of the LiDAR-based model (made available by the authors), for pixels that intersected the plots.

2.3. Statistical analyses

2.3.1. Assessment of map predictive power at plot locations

We compared the LiDAR-based biomass map predictions at plot locations (i.e., AGB_{map}) to field-based estimates (i.e., AGB_{field}) using the squared correlation between the two data sets (denoted R², eq. 2), a metric of bias (denoted B, eq. 3), the root mean square error (RMSE, eq. 4) and the coefficient of variation (CV, eq. 5).

$$R^2 = Cor\left(AGB_{map}, AGB_{field}\right)^2 \quad \text{(eq. 2)} \tag{2}$$

$$B = \frac{\left(\widehat{AGB_{map}} - \widehat{AGB_{field}}\right)}{\widehat{AGB_{field}}} \quad \text{(eq. 3)} \tag{3}$$

$$RMSE = \sqrt{\frac{1}{n} * \sum_1^n \left(AGB_{map,i} - AGB_{field,i}\right)^2} \quad \text{(eq. 4)} \tag{4}$$

$$CV = \frac{RMSE}{\widehat{AGB_{field}}} \quad \text{(eq. 5)} \tag{5}$$

With n the number of sample plots, $AGB_{map,i}$ and $AGB_{field,i}$ respectively the biomass of plot i extracted from the map and derived from field data, and $\widehat{AGB_{map}}$ and $\widehat{AGB_{field}}$ their mean across the n plots.

While AGB_{field} are assumed to be of greater quality (that is, of greater accuracy) [26] than AGB_{map}, both set of predictions are subject to a non-negligible uncertainty. In section '*Aboveground biomass estimation from inventory data*', we described the Monte Carlo procedure used to generate 1,000 AGB replicates by plot incorporating and allowing to quantify the uncertainty on AGB_{field}. The uncertainty on map AGB predictions have also been made available at pixel level in [18], and can be aggregated among pixels intersected by each plot (SE_{plot}) using standard error propagation rules. To account for the imperfect nature of AGB predictions when evaluating the LiDAR-based map, statistics of map predictive power (i.e., R², B, RMSE and CV) were computed by comparing each of the 1,000 plot AGB replicates (i.e., $AGB_{\geq 1cm}$) to a realization of AGB_{map}, defined as the sum of AGB_{map} to an error randomly drawn from the distribution N(0, $SE_{plot,i}$). This led to a vector of length 1,000 for each performance metric, from which we report the mean and its 95% confidence interval.

The temporal mismatch between the biomass map – which is representative of the early 2010s – and NFI data – which were acquired in 2017-2018 – may also introduce uncertainty in the assessment of map predictive power. For example, if a forested land was converted to a crop in the year 2015, the map would predict a high biomass for that land while the biomass estimation from NFI data would be low, hence resulting in a large prediction error for the map. This prediction error would therefore not reflect the predictive performance of the map but is attributable, in this example, to the 2015's land cover change. To further investigate the influence of this temporal mismatch, we used GLAD vegetation loss data [27] to remove all plots where one (or more) vegetation loss was detected in the 2010-2017 period. Map validation statistics were then computed using both the full set of 470 plots and the subset of unperturbed plots.

2.3.2. Design-based inference from the field sample plots and error propagation

AGB density per unit area for the whole area of study and for the subpopulations of interest were estimated using field plots data. The field plots were treated as a systematic cluster sample of size n = 122. The 122 elements in the sample represent all clusters in which at least one plot was accessible by the field crews and whose tree variables could be measured. The average AGB densities were estimated using ratio estimators [28,29], which are widely used for estimating population parameters in large-area forest surveys [30–34]. The ratio estimators were chosen because of the ability to accommodate cluster plots with partial nonresponse [35] and because they can be used efficiently for providing estimates for targeted subpopulations (also known as domains), such as forest types and administrative boundaries [34,36,37]. For estimation purposes, we assume that the set of nonresponse plots is missing at random, and they are not systematically different from the responding ones [38]. The population AGB density per unit area is estimated using the following ratio estimator (also known as ratio-to-size estimator [29,37,39]):

$$\hat{\mu}_{RATIO} = \frac{\sum_{j=1}^{n} AGB_{field,j}}{\sum_{j=1}^{n} a_{j}} \qquad \text{(eq. 6)} \qquad (6)$$

$$\widehat{Var}(\hat{\mu}_{RATIO}) = \frac{n}{(n-1)} \frac{\sum_{j=1}^{n}(AGB_{field,j} - a_{j}\hat{\mu}_{RATIO})^2}{\sum_{j=1}^{n}(a_{j})^2} \qquad \text{(eq. 7)} \qquad (7)$$

where n is the total sample size, $AGB_{field,j}$ is the aboveground biomass measured in the j[th] cluster and a_{j} is the area of the j[th] cluster which was accessible by the field crew. Averages by land use class and provinces are also estimated using the following domain ratio estimators:

$$\hat{R}_{d} = \frac{\sum_{j=1}^{n} AGB_{field,j,d}}{\sum_{j=1}^{n} a_{j,d}} \qquad \text{(eq. 8)} \qquad (8)$$

$$\widehat{Var}(\hat{R}_{d}) = \frac{n}{(n-1)} \frac{\sum_{j=1}^{n}(AGB_{field,j,d} - a_{,dj}\hat{\mu}_{RATIO})^2}{\sum_{j=1}^{n}(a_{j,d})^2} \qquad \text{(eq. 9)} \qquad (9)$$

where $AGB_{field,j,d}$ is the aboveground biomass measured in domain d and in the j[th] cluster and $a_{j,d}$ is the area of the j[th] cluster falling into domain d and that was accessible by the field crew. Despite the fact that $\widehat{Var}(\hat{\mu}_{RATIO})$ and $\widehat{Var}(\hat{R}_{d})$ from eq. 7 and eq. 9 may be biased when applied to systematic sampling, they are however likely to overestimate the variance [28], offering an acceptable conservative approach to the sample estimates. It is worthwhile to notice that the variance estimators (eq. 7 and eq. 9) account for the fact that both the aboveground biomass and the area measured are random variables.

The uncertainties arising from the missing inventory data, WD, H, and the allometric model obtained through the Monte Carlo simulation procedure described in section '*Aboveground biomass estimation from inventory data*' above, were propagated to the large-area estimates of mean AGB following the methodology provided by [38] (see also [40]). For each k^{th} Monte Carlo replication, the mean AGB, $\hat{\mu}^{k}$ and variance of the mean $\widehat{Var}(\hat{\mu}^{k})$ for the overall study area and for each domain were estimated using the ratio estimators (eq. 6) to (eq. 9) described above. The mean and variance over replications were estimated by

$$\hat{\mu} = \frac{1}{n_{rep}} \sum_{k=1}^{n_{rep}} \hat{\mu}^k \quad \text{(eq. 10)} \tag{10}$$

$$\widehat{Var}(\hat{\mu}) = (1 + 1/n_{rep})W_1 + W_2 \quad \text{(eq. 11)} \tag{11}$$

where n_{rep} is the number of replications, $W_1 = (n_{rep\,-1})^{-1} \sum_{k=1}^{n_{rep}} (\hat{\mu}^k - \hat{\mu})$ is the among replication variance and $W_2 = (n_{rep\,-1})^{-1} \sum_{k=1}^{n_{rep}} \widehat{Var}(\hat{\mu}^k)$ is the mean variance within replications.

2.3.3. Model-based inference from the biomass map

For calculation of mean biomass over large regions from the biomass map, we used the model-based estimator (MB) given in eq. 12, which simply consists of averaging map predictions over the region pixels.

$$\hat{\mu}_{MB} = \frac{1}{N} \times \sum_{i=1}^{N} AGB_{map,i} \quad \text{(eq. 12)} \tag{12}$$

where *i* indexes the pixels and N the total number of pixels within the region. We did not compute the variance of the MB estimate, which would require additional information on the biomass map, such as the spatial autocorrelation among the residuals, which were not available.

3. Results

3.1. Predictions of plot-to-plot biomass variation

3.1.1. Relationship between AGB_{MAP} and AGB_{FIELD} across all plots

Using the full set of 470 sample plots, we found that the map predicted 58 % of AGB_{FIELD} variation (Fig. 2-a) with an average prediction error (RMSE) of 103.6 Mg.ha^{-1} or 36.9 % (CV). The relationship between AGB_{FIELD} and AGB_{MAP} was slightly biased (slope of Major Axis regression: 1.16, 95% CI: 1.08-1.25), leading to a small underestimation of the biomass across plots (B = -2.4 %, Fig. 2-b). Removing plots where a loss of vegetation cover was detected between 2010 and the establishment of NFI sample plots (hereafter "perturbed plots", n = 59) did not lead to noticeable changes in the results (Fig. S1

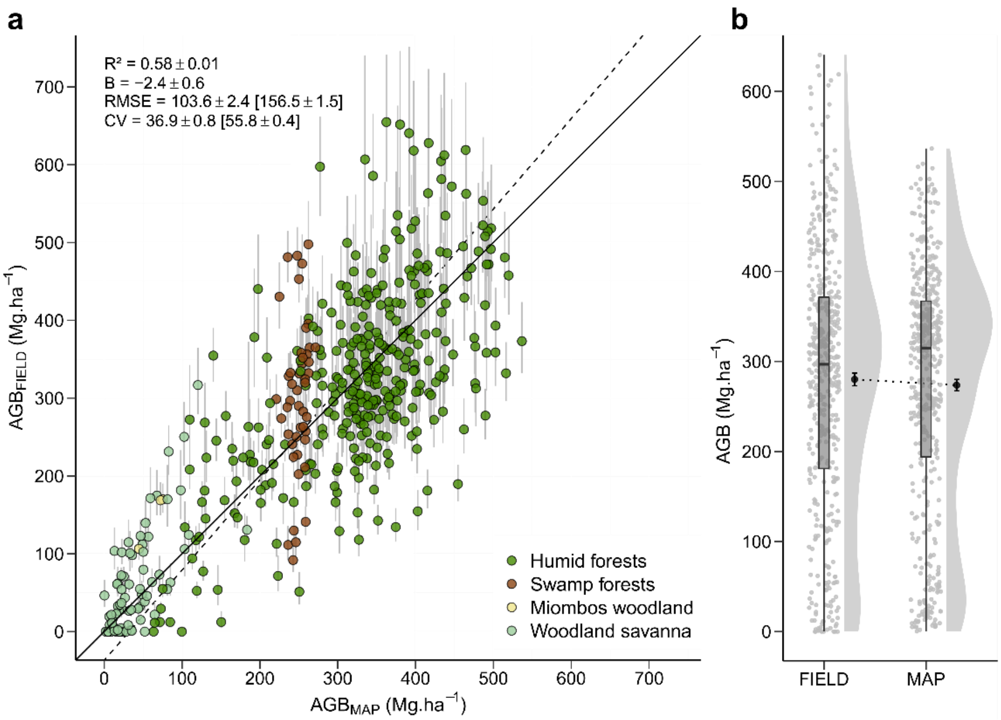

Figure 2. Relationship between sample plots aboveground biomass derived from inventory data (AGBFIELD) and from the biomass map (AGBMAP). a, Scatterplot of AGBFIELD vs AGBMAP. AGBFIELD estimates are bounded by their 95% confidence intervals including uncertainties arising from the simulation of missing inventory data, WD, H, and the allometric model (grey segments). The dash line represents the fit of a major axis regression. b, Distributions of AGBFIELD and AGBMAP. Distribution means are represented with thick circles (bounded by ± one s.e.). Dotted lines connect distribution means between data sources (i.e., forest inventories or biomass map).

3.1.2. Mapping error by classes of AGBFIELD

Breaking down the assessment of map prediction error by AGBFIELD classes of 50 Mg.ha^{-1} width, we found that map predictions were nearly unbiased on the early range of biomass (0 – 150 Mg.ha^{-1}, Fig. 3-a) which mostly comprised non-forest and open-canopy forest areas (Fig. 2-a). Beyond 150 Mg.ha^{-1}, map prediction error showed a non-linear pattern of bias. Across plots of intermediate biomass (c. 150 – 300 Mg.ha^{-1}), the map showed a moderate positive median error (c. 24.5 – 47.0 Mg.ha-1, Fig. 3-a). From 300 Mg.ha^{-1} onward, map prediction error decreased as AGBFIELD increased, becoming negative around c. 350 Mg.ha^{-1} and further decreasing up to the highest values of AGBFIELD, which were largely underestimated (median error : -234.6 Mg.ha^{-1}, n = 10). Removing perturbed plots unveiled a simpler bias pattern beyond 150 Mg.ha^{-1} consisting of a single linear decreasing trend (Fig. S2-a). This bias pattern suggests a loss of map predictive power on the second half of the AGBFIELD range. Using piecewise regression, we found a significant breakpoint in the AGBMAP – AGBFIELD relationship at 286 Mg.ha^{-1} (Davies' test $P < 0.0001$, Fig. 3-b) after which the linear correlation between AGBMAP and AGBFIELD was weak ($R^2 = 0.1$). The location of the breakpoint did not change when excluding perturbed plots (Fig. S2-b)

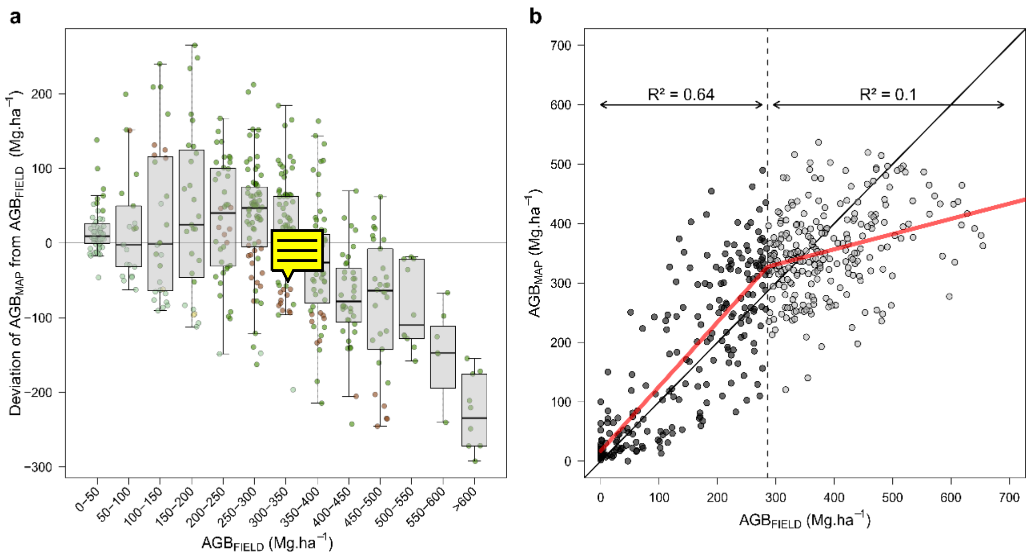

Figure 3. **a.,** Breakdown of mapping error by classes of aboveground biomass derived from inventory data (AGB_{FIELD}). **b.,** Breakpoint in the relationship between sample plots aboveground biomass derived from the biomass map (AGB_{MAP}) and AGB_{FIELD}. The red line represents the fit of a piecewise regression. The dashed vertical line highlights the location of the breakpoint.

3.1.3. Relationship between AGB_{MAP} and AGB_{FIELD} per landcover classes

We split the set of plots by landcover classes and assessed map predictive performance within classes, excluding the Miombos woodland class which only contained three plots.

Unsurprisingly, the map explained a greater share of AGB_{FIELD} variation in the low-biomass class of Woodland savanna ($R^2 = 0.41$) than in higher-biomass forest classes (Tab. 1). In the latter classes, the map captured 33% of AGB_{FIELD} variation within Humid forests, and did not discriminate any AGB variation within swamp forests (as seen in Fig. 2-a). This pattern of map predictive performance among landcover classes is consistent with the notion of signal saturation for higher AGB_{FIELD} values (ie. ≥ c. 290 Mg.ha^{-1}) and was strengthen when removing perturbed plots, with a higher predictive power on Woodland savanna ($R^2 = 0.58$) and a lower predictive power on humid forests ($R^2 = 0.20$, Tab. S1).

Table 1. Relationships between field- and map-derived plots aboveground biomass by land cover class.

Landcover	N	R^2	B	RMSE	CV
Woodland Savanna	77	0,41 ± 0,07	-33,3 ± 3,1	54,4 ± 3,2	94,9 ± 5,1
Swamp Forests	46	0,02 ± 0,03.	-17,6 ± 1,4	113,3 ± 4,4	37,4 ± 1,3
Humid Forests	344	0,33 ± 0,02	0,8 ± 0,7	110,5 ± 2,9	33,6 ± 0,9

It is noteworthy that map predictions on the set of NFI plots were virtually unbiased in humid forests (B < 1 %) but underestimated the average biomass of swamp forest plots by 17.5% and of woodland savanna plots by 33.2%. Removing perturbed plots accentuated the negative bias on the Woodland savanna class (B = -45.0 %, Tab. S1). Since map predictions were nearly unbiased on the early biomass range (0-150 Mg.ha^{-1}), the large underestimation of biomass in the woodland savanna class shows that this negative bias was in fact balanced-out by a positive bias on plots classified as forests (either Swamp or Humid) in this biomass range (Fig. 4-a). Landcover classification based on field observations made during the NFI showed that unperturbed plots classified as Woodland savanna by the landcover map corresponded in fact to a variety of non-forest classes. These classes are commonly found in the agro-mosaic landscape of central Africa, including savanna (37.0 %), crops (10.9 %), natural regeneration on abandoned crop (13.0 %) and mixes of non-forest (17.4 %) or non-forest and forest (21.7 %) classes (Fig. 4-b). Concerning unperturbed plots classified as Forest by the landcover map, most plots (i.e., 69.2 %) indeed corresponded to forests classes in the NFI classification (notably forests on hydromorphic soil) but with much lower biomass value than predicted by the map, while remaining plots were attributed to non-forest classes (Fig. 4-b), reflecting classification errors in the landcover map.

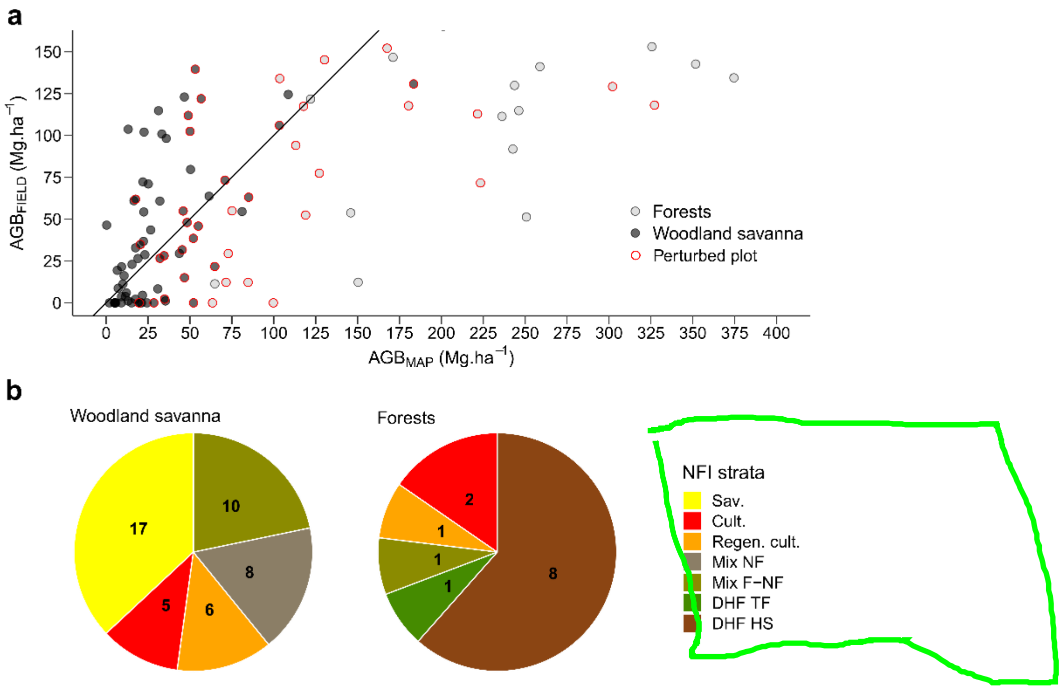

Figure 4. a., Relationship between sample plots aboveground biomass derived from inventory data (AGB_{FIELD}) and from the biomass map (AGB_{MAP}) in the early AGB range (i.e., 0 – 150 Mg.ha^{-1} of AGB_{FIELD}). Plot belonging to the woodland savanna or to a forest class are depicted in dark and light grey, respectively. Perturbed plots are highlighted with a red circle. **b.,** Pie charts showing the proportion of landcover classes from the NFI landcover classification found among plots belonging to the woodland savanna or to a forest class in the landcover map. Black number represent the number of plots by slice.

3.1.4. Predictions of mean biomass at population-level

We used the field sample plots to compute mean biomass estimates at different scales (i.e., the full study area, the land cover classes, the provinces) and contrasted these estimates to the ones obtained from the biomass map.

At the scale of the study area, the mean biomass estimate derived from field sample plots was 280.6 Mg.ha^{-1} and its 95 % CI (252.2 – 309.0 Mg.ha^{-1}) included the estimate derived from the map (i.e., 252.7 Mg.ha^{-1}, Fig. 5).

Among land cover classes, both data sources led to similar mean biomass estimates for the Humid forests class (i.e., 328.8 and 319.7 Mg.ha^{-1} for field sample plots and the map, respectively), but using field plots led to higher mean biomass estimates for Woodland savanna (i.e., 57.3 Mg.ha^{-1}, 95 % CI: 39.8 – 74.9 Mg.ha^{-1}) and Swamp forests classes (i.e., 302.7 Mg.ha^{-1}, 95 % CI: 251.6 – 353.7 Mg.ha^{-1}) than using the map (i.e., 31.8 and 247.8 Mg.ha^{-1}, respectively).

Among provinces, 95 % CIs around mean biomass estimates derived from field sample plots were large owing to the relatively small number of plots by provinces (range: 28 – 97 Mg.ha^{-1}, see Tab. S2 for details) and included mean biomass estimates from the map in six out of the nine provinces. At the province scale, the general trend observed is that using field sample plots led to higher mean biomass estimates as compared to estimates from the map. This observation is consistent with the results obtained with mean biomass estimates per land cover classes. In contrast, the mean biomass estimates for the Sud-Ubangui and Tshopo provinces were higher with the map than with field plots, indicating that the deviation between map and field mean biomass estimates differed in those provinces from the regional trend. In the Tshopo province for instance, where the Humid forest class covered 92.3 % of the land, the mean biomass estimate for that class was higher with the map (341.3 $Mg.ha^{-1}$) than with field sample plots (292.6 $Mg.ha^{-1}$, Fig. S3).

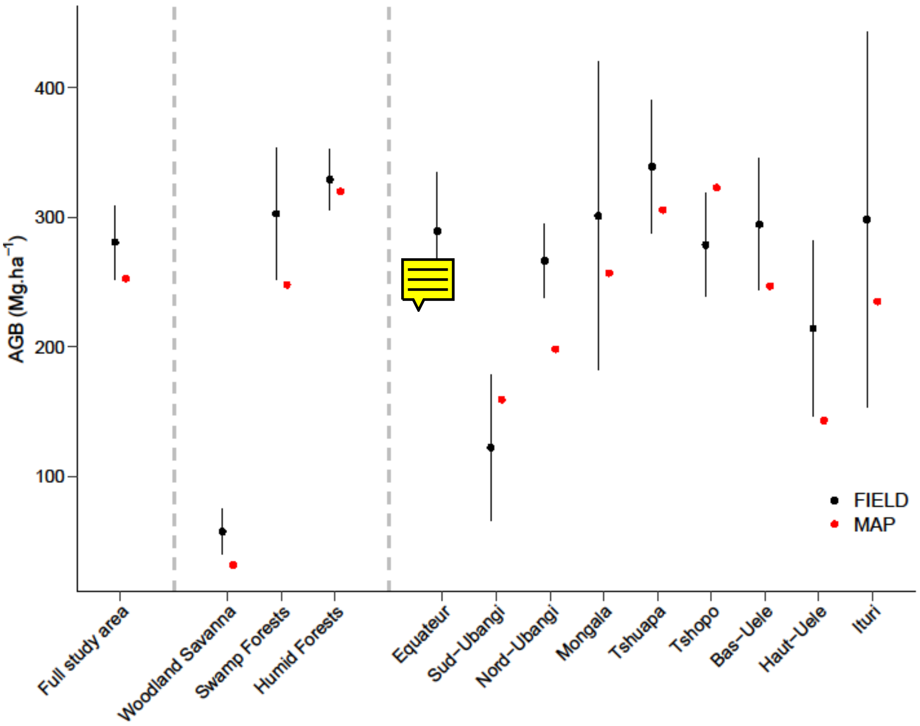

Figure 5. Mean biomass estimates at study area-, landcover class- and provincial-scale. Estimates from field data are bounded by a 95 % confidence interval. All confidence intervals include errors arising from sampling, missing inventory data, WD, H, and the allometric model. .

4. DISCUSSION

Validation of RS-derived maps is both essential to compare and improve mapping methodologies and to build confidence in mapping products and support their adoption by end-users [41]. Here, we performed an assessment of the LiDAR-based AGB map of DRC using NFI data regularly distributed over the northern part of the country, which hosts the majority of the Congo basin dense forests, an ecosystem on which AGB mapping is notoriously challenging. Our results show that the map predicts about 60% of plot-to-plot variation in field-derived AGB, but that its predictive performance is not homogeneous along the AGB gradient. Hereafter, we discuss our findings and their implications in using map-derived AGB in the context of REDD and forest management.

4.1. The overall relationship between RS- and field-derived AGB predictions is coherent

An important challenge when mapping forest AGB over a geographic extent as broad as the one covered by the DRC country (2.3 M km^2) is to build a prediction model that is sufficiently general i.e. that allows producing reliable AGB predictions in areas that are far apart model training data, which necessarily represent a very tiny fraction of the study area. To cope with the lack of field-derived reference data available to train RS models and the potential bias in their spatial distribution – which limits their representativity of the study area [42] –, it is increasingly recognized that a two-stage calibration strategy leveraging aerial LiDAR data is adequate [10,13]. In practice, the limited set of field inventory data is used to train aerial LiDAR data, and LiDAR-derived predictions are then used to calibrate the wall-to-wall RS model, which largely expands the size of the RS model training dataset. This strategy, which was used by [18], has been successfully employed on relatively small geographic areas (i.e., from a few hundreds to thousands km²), but implementations at country-scale and independent assessments of the resulting maps remain seldom (but see [43] for an implementation over Peru). Despite the vast geographic extent of DRC and the availability of only 92 1-ha plots clustered in a few sampling sites to calibrate the LiDAR-model, our results show that the mean deviation (or bias) of map AGB predictions at NFI plot locations is lower than 3%. Further, the LiDAR-based map explained about 60% of plot-to-plot variation in AGB across all plots, which is well within the range of results reported by local case studies using spatial cross-validation [14,44] and confirms the scalability of the two-stage calibration strategy.

4.2. The RS signal saturates on dense forests – but at relatively high AGB levels

While map validation statistics over the entire AGB gradient sampled by NFI plots were satisfying, we nonetheless observed a saturation phenomenon in the relationship between map- and field-derived AGB predictions around c. 290 $Mg.ha^{-1}$, above which the map's ability to predict plot-to-plot variation was weak ($R^2 = 0.1$). The saturation of multispectral imagers on high-biomass forest has been widely reported and the AGB threshold at which the loss of sensitivity occurs varies among sensors and forest types, notably. Interestingly, the saturation threshold found in this study is higher than that usually reported for Landsat data (100 – 200 $Mg.ha^{-1}$) [45] and even higher spatial resolution imagers (e.g. 250 $Mg.ha^{-1}$ for Worldview-3 [14]). We suggest that two main reasons explain this difference. First, Xu *et al.* used both Landsat and L-band ALOS PALSAR imagery to extrapolate LiDAR-derived predictions. The positive relationship between L-band backscatter and AGB have been widely-used in AGB mapping studies, which usually report an attenuation of the signal around c. 150 $Mg.ha^{-1}$. While this attenuation is interpreted as a complete loss of sensitivity (saturation), it has been shown that the relationship between L-band backscatter and forest AGB changes on dense forest canopies but could remain informative far beyond 150 $Mg.ha^{-1}$ [46]. It is thus possible that by using the MAXENT algorithm, which accommodates for non-linear relationships between model's covariates and the dependent variable, the inclusion of L-band radar in the mapping model allowed widening its range of sensitivity. Second, Xu *et al*'s mapping methodology consisted in separately mapping forest canopy height and stand wood density prior to fusing the two maps into an AGB map. In contrast with the more common methodology which consists in directly relating spaceborne data to forest AGB, the indirect approach used in [18] may better model variation in forest structure – through canopy height – and *in fine* capture more spatial variability in AGB. Indeed, variation in stand wood density among field sample plots may had a "noise" in field-derived AGB predictions that cannot be predicted by the mapping model, as current wall-to-wall spaceborne sensors have shown some sensitivity to variation in forest structure – such as forest canopy height [47] – while mapping wood density remain challenging [48].

4.3. The map shows contrasted performances within landcover classes

We used a simple landcover classification composed of two classes of forests (Humid and Swamp) and a single non-forest class (Woodland savannas) to disaggregate the map predictive performance by landcover classes. Given the non-homogenous performance of the map along the AGB gradient (i.e. saturation) and the structuration of landcover classes along this gradient, we naturally observed contrasted map performances per landcover classes.

The mean biomass for forest classes (i.e., 303 and 329 $Mg.ha^{-1}$ for Swamp and Humid forests, Tab. S2) were above the saturation threshold of the spaceborne mapping model leading to a weak correlation between map predictions and field-derived AGB predictions, with R^2s of 0.20 and 0.02 on Humid and Swamp forests (after excluding perturbed plots, Tab. S1), respectively. While map predictions were unbiased on the Humid forest class (B < 1 %), which cover most of our study area, we observed a systematic underestimation of Swamp forests AGB (c. -17.6%, Tab. S1). We suspect that the relatively poorer performance of the map on Swamp over Humid forests, both in terms of ability to capture the AGB gradient and the mean of the distribution, is related to the lack of field sample plots from this forest class in the training set of the LiDAR-based mapping model (i.e. a single Swamp forest plot, information communicated by the authors). Since swamp forests are clearly discernable from *terra firme* forest in optical very high resolution spaceborne data, and given the influence of humidity on the RADAR signal, it is indeed likely that relationships between model's covariates and forest AGB differs among Swamp and Humid forests.

As expected, the map showed a much higher predictive power on plot-to-plot AGB variation in Woodland savannas (R^2 = 0.58, Tab. S1), where the mean plot AGB (i.e., 57.3 $Mg.ha^{-1}$, Tab. S2) was much lower than the saturation threshold of the mapping model. While a common bias pattern in biomass mapping models is to over-estimate low AGB values and to under-estimate of high-AGB value [14,15], map predictions were – at first glance – nearly unbiased below the model saturation threshold. However, decomposing map predictive performance by landcover classes revealed a more complex pattern of error among low-AGB plots, with a large under-estimation of AGB on Woodland savanna plots (B = -45%) and an over-estimation of AGB on forest plots in the range 0 – 150 $Mg.ha^{-1}$ (Fig. 4-a). A possible reason for the underestimation of vegetation AGB in Woodland savannas could be, again, an improper calibration of the LiDAR model due to a lack of field data, since only five plots located in savannas were available for model training.

4.4. Implications for DRC's carbon emissions reporting and outlooks

The recent availability of a NFI in DRC gives to the country, for the first time, the opportunity to estimate mean carbon stocks of landcover classes in a design-based inferential framework, which warrant the unbiasedness of the estimates [13].

Using a ratio estimator, we obtained an estimate of mean AGB for the dominant Humid forest class that was very close to the estimate derived from the LiDAR-based map, but mean AGB estimates for the two other landcover classes (i.e. Swamp forest and Woodland Savanna) differed markedly between the two data sources (Fig. 5). We thus do not recommend the use of the LiDAR-based map in a model-based inferential framework to compute landcover classes mean carbon stocks, and *in fine* national emission factors, for REDD+ MVR reporting. This is not to say that the current LiDAR-based map, or the tremendous investment made to acquire aerial LiDAR data over the country, cannot be valued in REDD+ framework.

The logical next step to this study would be to assess the usefulness of the current LiDAR-based map to reduce the uncertainty on landcover class mean carbon stocks when combined with (rather than separately from) NFI plots. For instance, the map could be leveraged to increase the precision of the AGB estimates in the context of design-based inference through model-assisted estimation [13], which still relies on the probabilistic nature of the NFI plot design and warrants unbiasedness of the resulting estimates, despite potential biases in the map. Such an approach has proven to reduce the standard error on mean carbon stocks by more than twofold on Miombo woodlands of Tanzania [49], for example. Auxiliary data coming from the LiDAR-based map can also be used to address the non-response in ground data collection, in combination with special estimation techniques such as weighting or imputation [38,50].

The current acquisition of GEDI data, together with the availability of NFI data, also open avenues to improve the DRC LiDAR-based carbon map. GEDI data for instance could be integrated in the AGB mapping chain in several ways, either in addition to aerial LiDAR data in the training dataset of the forest canopy height mapping model, or as an independent validation dataset. In the latter case, the independent set of GEDI canopy height measurements could be used to select the covariates of the mapping model so as to maximize its transferability in space [51]. Similarly, the large size of the NFI dataset, its regular distribution over DRC and its independence from the data used to build the LiDAR-based AGB map makes NFI data an ideal validation dataset both to refine the functional forms of models used to build the AGB map (i.e., canopy height and wood density mapping models) and to assess the uncertainty of the final AGB product. Last, we also suggest that the landcover map used in the AGB mapping chain should match the official landcover stratification used by DRC in its international greenhouse gas reporting, which would facilitate the adoption of the AGB map by the country.

Supplementary Materials:

Author Contributions: L.A., P.P. and K.L.J.P. conceived the study and led the writing of the paper. L.A., P.P. and B.L. analyzed the data. B.L., X.L. and S.S. commented on the analyses and provided critical inputs for the writing of the paper.

Funding: P.P. was supported by a postdoctoral grant from the Centre national d'études spatiales (CNES) and from the 3DForMod project. 3DForMod was funded in the framework of the ERA-NET FACCE ERA-GAS (ANR-17-EGAS-0002-01), which has received funding from the European Union's Horizon 2020 research and innovation program under Grant Agreement No. 696356.

Data Availability Statement:

Acknowledgments: We are deeply grateful to DRC's Ministère de l'Environnement et du Développement Durable (MEDD) for granting us access to the NFI's data. In particular, we would like to stress out the continuous and effective support of Mr Benjamin Toirambe Bamoninga, General Secretariat of MEDD for the NFI data use and access.

We would also like to dedicate this article to Mr André Kondjo Shoko who passed away recently as he has played a critical and central role for the achievement of the first ever DRC national forest inventory. In his position as Head of the Forest Inventory Division within the Direction des Inventaires et Aménagement Forestier (DIAF) of the MEDD, he has greatly contributed to all phases of the preparation and the realization of the fieldwork with an exemplary rigor and self-denial. Might the present article be a recognition of his immense and long-term engagement for improving the scientific knowledge and the management of DRC forests.

Conflicts of Interest: The authors declare no conflicts of interest.

References

1. Mitchard, E.T.A. The Tropical Forest Carbon Cycle and Climate Change. *Nature* **2018**, *559*, 527–534, doi:10.1038/s41586-018-0300-2.
2. Tyukavina, A.; Hansen, M.C.; Potapov, P.; Parker, D.; Okpa, C.; Stehman, S.V.; Kommareddy, I.; Turubanova, S. Congo Basin Forest Loss Dominated by Increasing Smallholder Clearing. *Sci. Adv.* **2018**, *4*, eaat2993, doi:10.1126/sciadv.aat2993.
3. *Niveau d'Emissions de Référence Des Forêts*; Ministère de l'Environnement et Développement Durable: République Démocratique du Congo, 2018;
4. Nations, U. World Population Prospects: The 2017 Revision, Key Findings and Advance Tables. *U. N. N. Y.* **2017**.
5. Kengoum Djiegni, F.; Pham, T.T.; Sonwa, D.J. Dix Ans de REDD+ Dans Un Contexte Politique Changeant En République Démocratique Du Congo. *CIFOR Infobrief* **2020**.
6. Sandker, M.; Crete, P.; Lee, D.; Sanz-Sanchez, M. *Considérations Techniques Relatives à l'établissement de Niveaux d'émissions de Référence Pour Les Forêts et/Ou Niveaux de Référence Pour Les Forêts Dans Le Contexte de La REDD+ Au Titre de La CCNUCC*; FAO.; 2016; ISBN 978-92-5-208841-7.
7. Nesha, M.K.; Herold, M.; De Sy, V.; Duchelle, A.E.; Martius, C.; Branthomme, A.; Garzuglia, M.; Jonsson, O.; Pekkarinen, A. An Assessment of Data Sources, Data Quality and Changes in National Forest Monitoring Capacities in the Global Forest Resources Assessment 2005-2020. *Environ. Res. Lett.* **2021**.
8. Herold, M.; Carter, S.; Avitabile, V.; Espejo, A.B.; Jonckheere, I.; Lucas, R.; McRoberts, R.E.; Næsset, E.; Nightingale, J.; Petersen, R. The Role and Need for Space-Based Forest Biomass-Related Measurements in Environmental Management and Policy. *Surv. Geophys.* **2019**, *40*, 757–778.
9. McRoberts, R.E.; Tomppo, E.O.; Næsset, E. Advances and Emerging Issues in National Forest Inventories. *Scand. J. For. Res.* **2010**, *25*, 368–381.
10. Réjou-Méchain, M.; Barbier, N.; Couteron, P.; Ploton, P.; Vincent, G.; Herold, M.; Mermoz, S.; Saatchi, S.; Chave, J.; de Boissieu, F. Upscaling Forest Biomass from Field to Satellite Measurements: Sources of Errors and Ways to Reduce Them. *Surv. Geophys.* **2019**, *40*, 881–911.
11. Rejou-Mechain, M.; Muller-Landau, H.C.; Detto, M.; Thomas, S.C.; Le Toan, T.; Saatchi, S.S.; Barreto-Silva, J.S.; Bourg, N.A.; Bunyavejchewin, S.; Butt, N.; et al. Local Spatial Structure of Forest Biomass and Its Consequences for Remote Sensing of Carbon Stocks. *BIOGEOSCIENCES* **2014**, *11*, 6827–6840.

12. Knapp, N.; Huth, A.; Fischer, R. Tree Crowns Cause Border Effects in Area-Based Biomass Estimations from Remote Sensing. *Remote Sens.* **2021**, *13*, 1592, doi:10.3390/rs13081592.
13. Duncanson, L.; Armston, J.; Disney, M.; Avitabile, V.; Barbier, N.; Calders, K.; Carter, S.; Chave, J.; Herold, M.; Macbean, N. *Aboveground Woody Biomass Product Validation Good Practices Protocol. Version 1.0.*; CEOS Working Group on Calibration and Validation. Lanf Product Validation …, 2021;
14. Jha, N.; Tripathi, N.K.; Barbier, N.; Virdis, S.G.; Chanthorn, W.; Viennois, G.; Brockelman, W.Y.; Nathalang, A.; Tongsima, S.; Sasaki, N. The Real Potential of Current Passive Satellite Data to Map Aboveground Biomass in Tropical Forests. *Remote Sens. Ecol. Conserv.* **2021**.
15. Xu, L.; Saatchi, S.S.; Yang, Y.; Yu, Y.; White, L. Performance of Non-Parametric Algorithms for Spatial Mapping of Tropical Forest Structure. *Carbon Balance Manag.* **2016**, *11*, 18, doi:10.1186/s13021-016-0062-9.
16. Mitchard, E.T.; Saatchi, S.S.; Baccini, A.; Asner, G.P.; Goetz, S.J.; Harris, N.L.; Brown, S. Uncertainty in the Spatial Distribution of Tropical Forest Biomass: A Comparison of Pan-Tropical Maps. *Carbon Balance Manag.* **2013**, *8*, 10.
17. Langner, A.; Achard, F.; Grassi, G. Can Recent Pan-Tropical Biomass Maps Be Used to Derive Alternative Tier 1 Values for Reporting REDD+ Activities under UNFCCC? *Environ. Res. Lett.* **2014**, *9*, 124008.
18. Xu, L.; Saatchi, S.S.; Shapiro, A.; Meyer, V.; Ferraz, A.; Yang, Y.; Bastin, J.-F.; Banks, N.; Boeckx, P.; Verbeeck, H.; et al. Spatial Distribution of Carbon Stored in Forests of the Democratic Republic of Congo. *Sci. Rep.* **2017**, *7*, 15030, doi:10.1038/s41598-017-15050-z.
19. Saatchi, S.; Mascaro, J.; Xu, L.; Keller, M.; Yang, Y.; Duffy, P.; Espírito-Santo, F.; Baccini, A.; Chambers, J.; Schimel, D. Seeing the Forest beyond the Trees. *Glob. Ecol. Biogeogr.* **2015**, *24*, 606–610, doi:10.1111/geb.12256.
20. Chave, J.; Coomes, D.; Jansen, S.; Lewis, S.L.; Swenson, N.G.; Zanne, A.E. Towards a Worldwide Wood Economics Spectrum. *Ecol. Lett.* **2009**, *12*, 351–366.
21. Zanne, A.E.; Lopez-Gonzalez, G.; Coomes, D.A.; Ilic, J.; Jansen, S.; Lewis, S.L.; Miller, R.B.; Swenson, N.G.; Wiemann, M.C.; Chave, J. Data from: Towards a Worldwide Wood Economics Spectrum. **2009**.
22. Beirne, C.; Miao, Z.; Nuñez, C.L.; Medjibe, V.P.; Saatchi, S.; White, L.J.T.; Poulsen, J.R. Landscape-level Validation of Allometric Relationships for Carbon Stock Estimation Reveals Bias Driven by Soil Type. *Ecol. Appl.* **2019**, *29*, e01987.
23. Ploton, P.; Mortier, F.; Barbier, N.; Cornu, G.; Réjou-Méchain, M.; Rossi, V.; Alonso, A.; Bastin, J.-F.; Bayol, N.; Bénédet, F.; et al. A Map of African Humid Tropical Forest Aboveground Biomass Derived from Management Inventories. *Sci. Data* **2020**, *7*, 221, doi:10.1038/s41597-020-0561-0.

24. Chave, J.; Réjou-Méchain, M.; Búrquez, A.; Chidumayo, E.; Colgan, M.S.; Delitti, W.B.; Duque, A.; Eid, T.; Fearnside, P.M.; Goodman, R.C.; et al. Improved Allometric Models to Estimate the Aboveground Biomass of Tropical Trees. *Glob. Change Biol.* **2014**, *20*, 3177–3190.

25. Johnson, C.E.; Barton, C.C. Where in the World Are My Field Plots? Using GPS Effectively in Environmental Field Studies. *Front. Ecol. Environ.* **2004**, *2*, 475–482.

26. McRoberts, R.E.; Næsset, E.; Liknes, G.C.; Chen, Q.; Walters, B.F.; Saatchi, S.; Herold, M. Using a Finer Resolution Biomass Map to Assess the Accuracy of a Regional, Map-Based Estimate of Forest Biomass. *Surv. Geophys.* **2019**, doi:10.1007/s10712-019-09507-1.

27. Hansen, M.C.; Potapov, P.V.; Moore, R.; Hancher, M.; Turubanova, S.A.; Tyukavina, A.; Thau, D.; Stehman, S.V.; Goetz, S.J.; Loveland, T.R.; et al. High-Resolution Global Maps of 21st-Century Forest Cover Change. *science* **2013**, *342*, 850–853.

28. Sarndal, C. Särndal, C.-E., Swensson, B., and Wretman, J., Model Assisted Survey Sampling. Springer-Verlag, New York, 1992. ISBN 0-387-97528-4. Xv--694 Pp. S4900. Survey Sampling Is a Universally. *J. Off. Stat.* **1992**, *8*, 241–246.

29. Cochran, W. am G. Sampling Techniques, John Weily and Sons Inc. *N. Y.* **1977**, 135.

30. Scott, C.T.; Bechtold, W.A.; Reams, G.A.; Smith, W.D.; Hansen, M.H.; Moisen, G.G. Sample-Based Estimators Utilized by the Forest Inventory and Analysis National Information Management System. *Enhanc. For. Inventory Anal. Program. Sampl. Des. Estim. Proced. Ed. WA Bechtold PL Patterson USDA For. Serv. South. Res. Stn. Asheville N. C.* **2004**, 43–68.

31. Tomppo, E. The Finnish National Forest Inventory. In: McRoberts, Ronald E.; Reams, Gregory A.; Van Deusen, Paul C.; McWilliams, William H., Eds. Proceedings of the Eighth Annual Forest Inventory and Analysis Symposium; 2006 October 16-19; Monterey, CA. Gen. Tech. Report WO-79. Washington, DC: U.S. Department of Agriculture, Forest Service. 39-46. 2009.

32. Thompson, S.K. *Sampling, Third Edition*; John Wiley & Sons Inc: Hoboken, USA, 2012;

33. Korhonen, K.T.; Salmensuu, O. *Formulas for Estimators and Their Variances in NFI*; Internal report. United States Department of Agriculture, Washington, DC …, 2014;

34. Henry, M.; Iqbal, Z.; Johnson, K.; Akhter, M.; Costello, L.; Scott, C.; Jalal, R.; Hossain, M.A.; Chakma, N.; Kuegler, O. A Multi-Purpose National Forest Inventory in Bangladesh: Design, Operationalisation and Key Results. *For. Ecosyst.* **2021**, *8*, 1–22.

35. Espejo, A.; Federici, S.; Green, C.; Amuchastegui, N.; d'Annunzio, R.; Balzter, H.; Bholanath, P.; Brack, C.; Brewer, C.; Birigazzi, L. Integration of Remote-Sensing and Ground-Based Observations for Estimation of Emissions and Removals of Greenhouse Gases in Forests: Methods and Guidance from the Global Forest Observations Initiative, Edition 3.0. *Rome Italy UN Food Agric. Organ. 300 P* **2020**.

36. Birigazzi, L.; Gamarra, J.G.P.; Gregoire, T.G. Unbiased Emission Factor Estimators for Large-Area Forest Inventories: Domain Assessment Techniques. *Environ. Ecol. Stat.* **2018**, *25*, 199–219, doi:10.1007/s10651-018-0397-3.

37. Scott, C.T. *Estimation Using Ratio-to-Size Estimator across Strata and Subpopulations*; 2020;

38. Rubin, D.B. *Multiple Imputation for Survey Nonresponse*; New York: Wiley, 1987;

39. Hossain, M.A.; Aziz, A.; Chakma, N.; Johnson, K.; Henry, M.; Jalal, R.; Carrillo, O.; Scott, C.; Birigazzi, L.; Akhter, M.; et al. *Estimation Procedures of Indicators and Variables of the Bangladesh Forest Inventory*; Forest Department and Food and Agricultural Organization of the United Nations: Dhaka, Bangladesh, 2019;

40. McRoberts, R.E.; Westfall, J.A. Propagating Uncertainty through Individual Tree Volume Model Predictions to Large-Area Volume Estimates. *Ann. For. Sci.* **2016**, *73*, 625–633.

41. Perugini, L.; Pellis, G.; Grassi, G.; Ciais, P.; Dolman, H.; House, J.I.; Peters, G.P.; Smith, P.; Günther, D.; Peylin, P. Emerging Reporting and Verification Needs under the Paris Agreement: How Can the Research Community Effectively Contribute? *Environ. Sci. Policy* **2021**, *122*, 116–126, doi:10.1016/j.envsci.2021.04.012.

42. Marvin, D.C.; Asner, G.P.; Knapp, D.E.; Anderson, C.B.; Martin, R.E.; Sinca, F.; Tupayachi, R. Amazonian Landscapes and the Bias in Field Studies of Forest Structure and Biomass. *Proc. Natl. Acad. Sci.* **2014**, *111*, E5224–E5232, doi:10.1073/pnas.1412999111.

43. Csillik, O.; Kumar, P.; Mascaro, J.; O'Shea, T.; Asner, G.P. Monitoring Tropical Forest Carbon Stocks and Emissions Using Planet Satellite Data. *Sci. Rep.* **2019**, *9*, 1–12.

44. Sagang, L.B.T.; Ploton, P.; Sonké, B.; Poilvé, H.; Couteron, P.; Barbier, N. Airborne Lidar Sampling Pivotal for Accurate Regional AGB Predictions from Multispectral Images in Forest-Savanna Landscapes. *Remote Sens.* **2020**, *12*, 1637, doi:10.3390/rs12101637.

45. Lu, D.; Chen, Q.; Wang, G.; Liu, L.; Li, G.; Moran, E. A Survey of Remote Sensing-Based Aboveground Biomass Estimation Methods in Forest Ecosystems. *Int. J. Digit. Earth* **2016**, *9*, 63–105.

46. Mermoz, S.; Réjou-Méchain, M.; Villard, L.; Le Toan, T.; Rossi, V.; Gourlet-Fleury, S. Decrease of L-Band SAR Backscatter with Biomass of Dense Forests. *Remote Sens. Environ.* **2015**, *159*, 307–317, doi:10.1016/j.rse.2014.12.019.

47. Hansen, M.C.; Potapov, P.V.; Goetz, S.J.; Turubanova, S.; Tyukavina, A.; Krylov, A.; Kommareddy, A.; Egorov, A. Mapping Tree Height Distributions in Sub-Saharan Africa Using Landsat 7 and 8 Data. *Remote Sens. Environ.* **2016**, *185*, 221–232, doi:10.1016/j.rse.2016.02.023.
48. Phillips, O.L.; Sullivan, M.J.; Baker, T.R.; Mendoza, A.M.; Vargas, P.N.; Vásquez, R. Species Matter: Wood Density Influences Tropical Forest Biomass at Multiple Scales. *Surv. Geophys.* **2019**, *40*, 913–935.
49. Næsset, E.; McRoberts, R.E.; Pekkarinen, A.; Saatchi, S.; Santoro, M.; Trier, Ø.D.; Zahabu, E.; Gobakken, T. Use of Local and Global Maps of Forest Canopy Height and Aboveground Biomass to Enhance Local Estimates of Biomass in Miombo Woodlands in Tanzania. *Int. J. Appl. Earth Obs. Geoinformation* **2020**, *89*, 102109, doi:10.1016/j.jag.2020.102109.
50. McRoberts, R.E. Compensating for Missing Plot Observations in Forest Inventory Estimation. *Can. J. For. Res.* **2003**, *33*, 1990–1997.
51. Meyer, H.; Reudenbach, C.; Wöllauer, S.; Nauss, T. Importance of Spatial Predictor Variable Selection in Machine Learning Applications–Moving from Data Reproduction to Spatial Prediction. *Ecol. Model.* **2019**, *411*, 108815.

SUPPLEMENTARY FIGURES

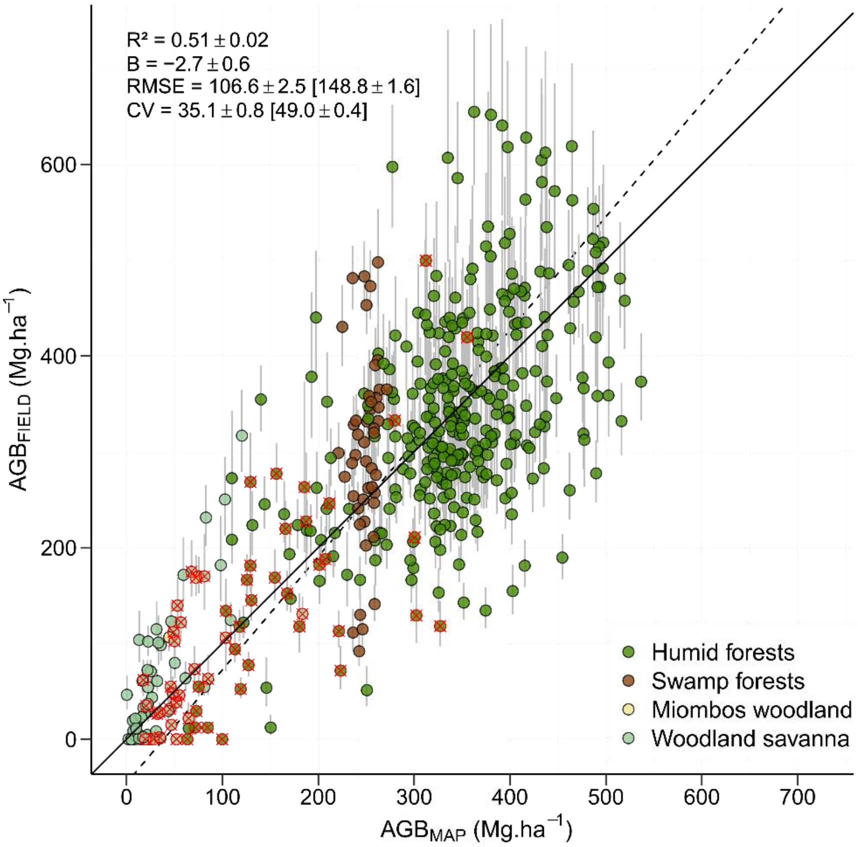

Figure S1. Scatterplot of sample plots aboveground biomass derived from inventory data (AGB_{FIELD}) and vs the biomass map (AGB_{MAP}). AGB_{FIELD} estimates are bounded by their 95% confidence interval (grey segments). The dash line represents the fit of a major axis regression. For information, perturbed plots are highlighted by red crossed circles, but these plots were not used when computing map performance statistics and fitting the major axis regression model.

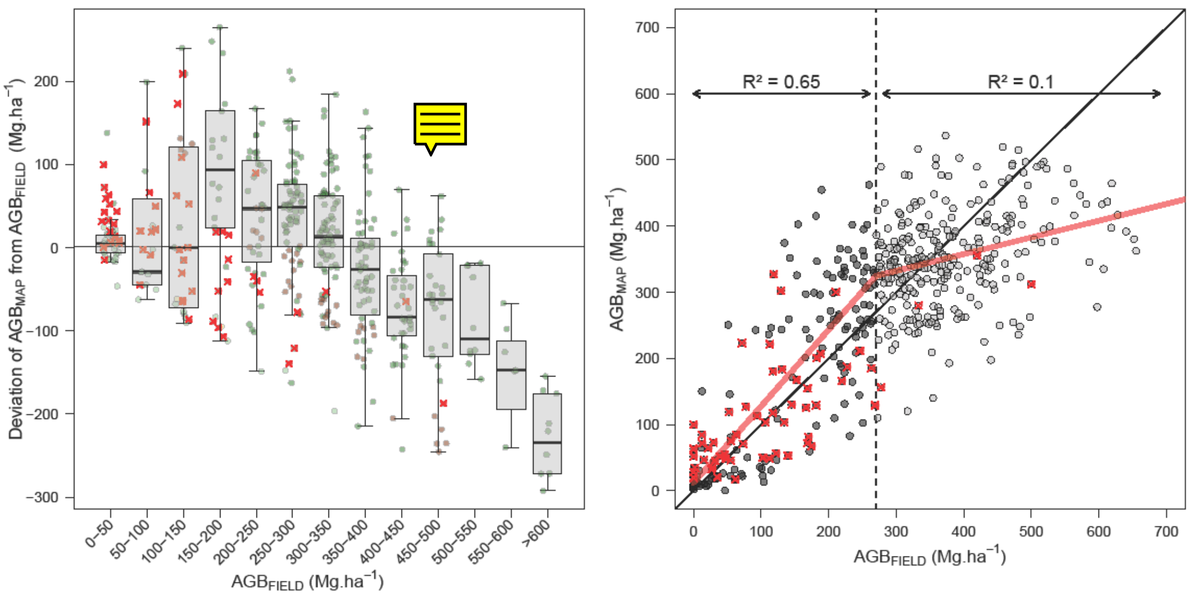

Figure S2. a., Breakdown of mapping error by classes of aboveground biomass derived from inventory data (AGB_{FIELD}). **b.,** Breakpoint in the relationship between sample plots aboveground biomass derived from the biomass map (AGB_{MAP}) and AGB_{FIELD}. The red line represents the fit of a piecewise regression. The dashed vertical line highlights the location of the breakpoint. For information, perturbed plots in **a** and **b** are highlighted by red crossed circles, but are not used when generating boxes (**a**) or fitting the pricewise regression (**b**).

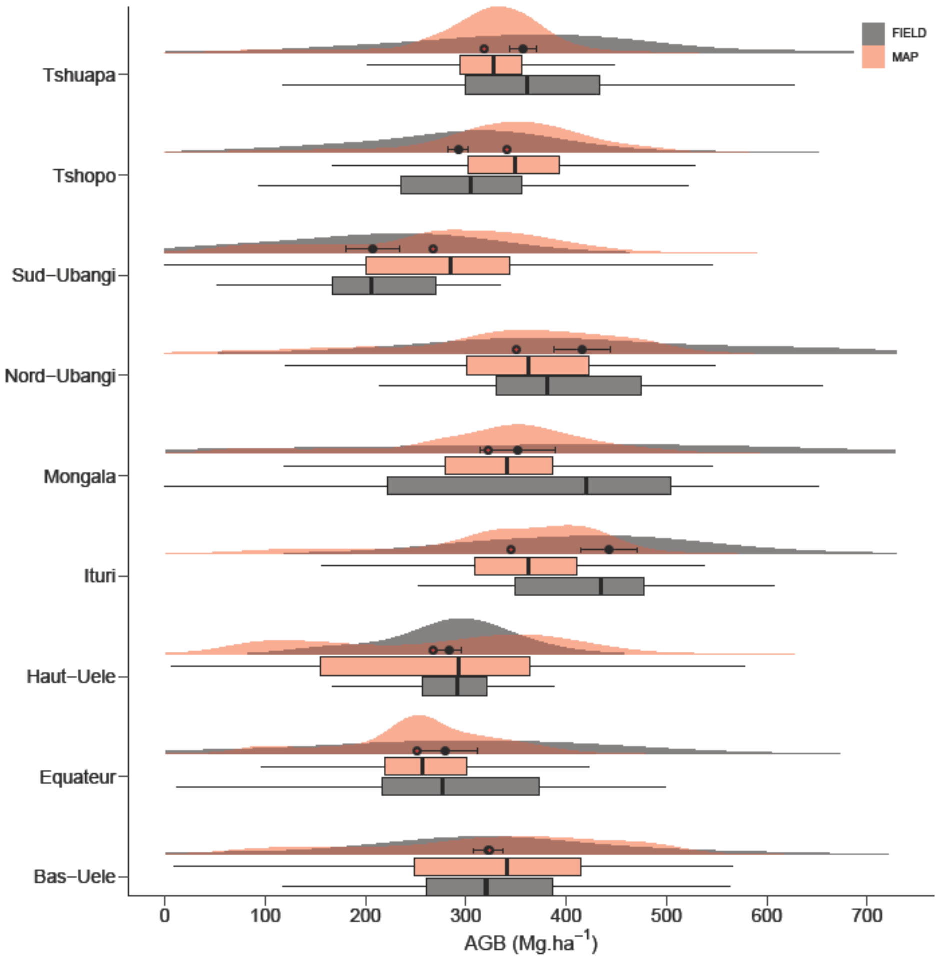

Figure S3. Provincial distributions of aboveground biomass (AGB) in field sample plots (red) and in the map (dark grey) for the Humid forests class. Distribution means are represented with thick circles (bounded by ± one s.e.).

SUPPLEMENTARY TABLES

Table S1. Relationships between field- and map-derived plots aboveground biomass by land cover class. Perturbed plots were removed from the analysis.

Landcover	N	R^2	B	RMSE	CV
Woodland Savanna	52	0.58 ± 0.09	-45.0 ± 3.3	56.7 ± 4.1	104.9 ± 6.8
Swamp Forests	46	0.02 ± 0.03	-17.5 ± 1.3	113.1 ± 4.3	37.4 ± 1.3
Humid Forests	311	0.20 ± 0.02	0.5 ± 0.7	111.9 ± 3.1	32.3 ± 0.9

Table S2. Mean biomass estimation (in $Mg.ha^{-1}$) by stratum using field sample plots and the biomass map.

Stratum	FIELD			MAP
	n	AGB	95% CI	AGB
Study area	470	280.6	252.2 – 309.0	252,7
Woodland Savanna	77	57.3	39.8 – 74.9	31,8
Swamp Forests	46	302.7	251.6 – 353.7	247,8
Humid Forests	344	328.8	305.4 – 352.2	319,7
Nord-Ubangi	32	266.3	117.3 – 415.2	198,2
Bas-Uele	77	294.5	244.0 – 345.0	246,8
Sud-Ubangi	28	122.4	65.9 – 178.8	159,3
Haut-Uele	32	214.1	146.6 – 281.6	143,2
Ituri	36	297.9	153.4 – 442.4	234,9
Mongala	36	300.9	181.9 – 419.8	256,8
Equateur	58	289.1	243.4 – 334.7	239,5
Tshopo	97	278.5	238.9 – 318.0	322,7
Tshuapa	74	338.9	287.4 – 390.5	305,5